# Latent Heat Fluxes Through Soft Materials With Microtruss Architectures

**Matthew J. Traum**
Institute for Soldier Nanotechnologies,
Massachusetts Institute of Technology,
77 Massachusetts Avenue,
Cambridge, MA 02139;
Department of Mechanical Engineering,
Massachusetts Institute of Technology,
77 Massachusetts Avenue,
Cambridge, MA 02139

**Peter Griffith**
Department of Mechanical Engineering,
Massachusetts Institute of Technology,
77 Massachusetts Avenue,
Cambridge, MA 02139

**Edwin L. Thomas**
Institute for Soldier Nanotechnologies,
Massachusetts Institute of Technology,
77 Massachusetts Avenue,
Cambridge, MA 02139;
Department of Materials Science and Engineering,
Massachusetts Institute of Technology,
77 Massachusetts Avenue,
Cambridge, MA 02139

**William A. Peters**[1]
Institute for Soldier Nanotechnologies,
Massachusetts Institute of Technology,
77 Massachusetts Avenue,
Cambridge, MA 02139
e-mail: peters@mit.edu

*Microscale truss architectures provide high mechanical strength, light weight, and open porosity in polymer sheets. Liquid evaporation and transport of the resulting vapor through truss voids cool nearby surfaces. Thus, microtruss materials can simultaneously prevent mechanical and thermal damage. Assessment of promise requires quantitative understanding of vapor transport through microtruss pores for realistic heat loads and latent heat carriers. Pore size may complicate exegesis owing to vapor rarefaction or surface interactions. This paper quantifies the nonboiling evaporative cooling of a flat surface by water vapor transport through two different hydrophobic polymer membranes,* $112–119\ \mu m$ *(or* $113–123\ \mu m$*) thick, with microtruss-like architectures, i.e., straight-through pores of average diameter of* $1.0–1.4\ \mu m$ *(or* $12.6–14.2\ \mu m$*) and average overall porosity of 7.6% (or 9.9%). The surface, heated at* $1350 \pm 20\ W_t/m^2$ *to mimic human thermal load in a desert (daytime solar plus metabolic), was the bottom of a* $3.1\ cm$ *inside diameter,* $24.9\ cm^3$ *cylindrical aluminum chamber capped by the membrane. Steady-state rates of water vapor transport through the membrane pores to ambient were measured by continuously weighing the evaporation chamber. The water vapor concentration at the membrane exit was maintained near zero by a cross flow of dry nitrogen* $(velocity=2.8\ m/s)$*. Each truss material enabled* $13–14°C$ *evaporative cooling of the surface, roughly 40% of the maximum evaporative cooling attainable, i.e., with an uncapped chamber. Intrinsic pore diffusion coefficients for dilute water vapor* $(<10.4$ *mole* $\%)$ *in air (P total* $\sim$*112,000 Pa) were deduced from the measured vapor fluxes by mathematically disaggregating the substantial mass transfer resistances of the boundary layers* $(\sim 50\%)$ *and correcting for radial variations in upstream water vapor concentration. The diffusion coefficients for the* $1.0–1.4\ \mu m$ *pores (Knudsen number* $\sim 0.1$*) agree with literature for the water vapor-air mutual diffusion coefficient to within* $\pm 20\%$*, but for the nominally* $12.6–14.2\ \mu m$ *pores (Kn* $\sim 0.01$*), the diffusion coefficient values were smaller, possibly because considerable pore area resides in noncircular, i.e., narrow, wedge-shaped cross sections that impede diffusion owing to enhanced rarefaction. The present data, parameters, and mathematical models support the design and analysis of microtruss materials for thermal or simultaneous thermal-and-mechanical protection of microelectromechanical systems, nanoscale components, humans, and other macrosystems.* [DOI: 10.1115/1.2818760]

*Keywords: microtruss, architecture, latent, heat transfer, mass transfer, pore, diffusion, MEMS, nanotechnology, membrane, polymers, soft materials, evaporation, nonboiling, evaporative cooling, phase change, surface, interface, thermal management, systems integration*

## Introduction

Microtrusses, also known as microframes [1], are polymeric sheetlike structures whose ordered networks of micro- to nanoscale rods, struts, cells, and channels mimic the high strength-to-weight ratio of macroscale trusses used in the construction of bridges, towers, and buildings. Microtrusses provide light weight, high porosity, and extraordinary absorption of mechanical energy without rupture in a single material [2]. Moreover, microtrusses can manipulate heat transmission by modifying the transport of latent heat-carrying vapors. Thus, microtruss architectures have the potential to simultaneously protect humans and inanimate objects from mechanical and thermal damage. Assessment of viability requires that vapor transport within truss pores and the resulting latent heat transmission be quantified for practical thermal loads and latent heat carriers, and be compared with thermal conduction across the truss. There is also a need to determine if smaller pore widths affect vapor transport owing to vapor rarefaction or surface interactions [3–5].

Mass transfer through porous structures has been studied owing, inter alia, to diverse practical applications [6], e.g., catalytic reaction engineering [7], textile comfort [8], fluid permeation of concrete [9], sintered metals and packed beds [10], and separation processes, such as desalination [11] and gas purification [12–14]. Selected examples include measurements of rates of water evaporation into air-filled pores of glass fiber and Teflon™ membranes separating saline and fresh water [11] and studies of drying and cooling with cotton [15]. Johnson et al. [16] studied the potential of polypropylene membranes with 30–100 nm pores to act as multifunctional protective barriers, i.e., to filter bacteria from water and then cool indoor air by evaporating the resulting decontaminated liquid. Gibson et al. [17] studied transport in porous

[1]Corresponding author.

Contributed by the Heat Transfer Division of ASME for publication in the Journal of Heat Transfer. Manuscript received July 31, 2006; final manuscript received June 20, 2007; published online March 17, 2008. Review conducted by Gang Chen. Paper presented at the ASME 2006 Energy Nanotechnology International Conference (ENIC2006), Boston, MA, June 26–28, 2006.

  

Table 1 Operating parameters and structural properties of the various barrier materials used in measurements of latent heat transmission

| Overlay | Porosity (%) | Av. pore diameter ($\mu$m) | Thickness ($\mu$m) | Av. $T_3$ (K) | Av. $T_2$ (K) | Av. $\rho_2$ (kg/m$^3$) | Mole % $H_2O$ vapor (%) | $\Delta m/\Delta t$ (kg/s) |
|---|---|---|---|---|---|---|---|---|
| Nucrel®, Sample A | $7.6 \pm 2.5$ | $1.0 \pm 0.2$ | $112 \pm 3$ | 302.7 | 316.1 | 0.059 | 8.531 | $5.07E-07$ |
| Nucrel®, Sample B | $7.5 \pm 3.3$ | $1.4 \pm 0.2$ | $119 \pm 4$ | 301.9 | 315.0 | 0.056 | 8.049 | $5.98E-07$ |
| Hytrel®, Sample A | $11.2 \pm 3.1$ | $14.2 \pm 1.6$ | $113 \pm 3$ | 302.1 | 313.3 | 0.052 | 7.363 | $5.97E-07$ |
| Hytrel®, Sample B | $8.6 \pm 2.7$ | $12.6 \pm 1.5$ | $123 \pm 3$ | 305.8 | 314.7 | 0.055 | 7.907 | $4.62E-07$ |
| Nonporous latex | 0 | N/A | $141 \pm 3$ | 316.8 | 334.4 | 0.127 | 19.292 | 0 |
| No Membrane | 100 | N/A | N/A | N/A | N/A | N/A | N/A | $(1.26 \pm 0.08)E-06$ |

membranes fabricated from electrospun nylon 6,6 nanofibers to integrate hazardous substance protection with improved human thermal comfort by evaporation of sweat.

Complications may arise if length scales in a porous medium, e.g., pore width, are comparable to or less than the mean free path, de Broglie wavelength, etc. [18]. Physical transport of molecules may be impacted by fluid rarefaction [3,5,19,20], surface curvature [4,21], wetting [4], fluctuations in species concentration at interfaces [22], or surface topography, as seen in superheat requirements for boiling [23,24]. Such effects must be understood because they can give rise to heat and mass transfer behaviors dramatically different from those of macrosystems [18,25]. For example, unprecedented increases in flux densities of liquids and gases through channels with nanoscale widths have been measured [26,27]. The ability to sculpt and image highly reproducible micron and nanometer scale geometric features in hard and soft materials opens new opportunities for experiments to study effects of tiny length scales on heat and mass transfer in well-defined micro- and nanomedia. Progress in the theoretical understanding of heat transfer [18] and mass transfer [7,18,25,28] in condensed phase and micro-nanoscale flow systems over the last two decades facilitates interpretation of the resulting observations.

The above and other prior studies are valuable contributions but do not duplicate the present study of nonboiling latent heat transmission through soft materials with well-defined microtruss architectures. In particular, this paper quantifies water vapor transport rates through the pores of two different hydrophobic polymeric membranes with microtruss features and the resulting evaporative cooling of a nearby flat surface, heated at a flux density representative of the metabolic plus daytime desert solar load on a human. Heat balances close to within $\pm 12\%$ and thermal conduction across each microtruss were measured. To facilitate engineering design, an intrinsic (apparatus-independent) coefficient for pore diffusion of latent heat carrier was deduced for each microtruss simulant.

## Characterization of Microtruss Simulants and Other Barrier Materials

Zero-porosity latex was the negative control barrier material. Lacking actual microtrusses [29] of sufficient facial area, we studied two microtruss stand-ins prepared by the DuPont Company using DuPont proprietary technology: 112–119 $\mu$m (or 113–123 $\mu$m) thick Nucrel® (or Hytrel®) hydrophobic membranes with straight-through pores of equivalent average diameter of 1.0–1.4 $\mu$m (or 12.6–14.2 $\mu$m) and average overall porosity of 7.6% (or 9.9%). Nucrel® is a random copolymer of ethylene and methacrylic acid (12 wt %). Hytrel® is a random polyether-ester copolymer formed by the condensation of terephthalic acid, tetramethylene glycol, and polytetramethylene glycol. Pore diameters and total porosity (Table 1) were determined by image analysis using an open source software (IMAGEJ from NIH) of 400–500 scanning electron micrographs (SEMs) (Fig. 1). Each microtruss was cleaned before every imaging (or evaporation) run by flushing each face for 30 s with clean, dry nitrogen gas. Each specimen was divided into a grid of ~500 equally spaced nodes. The squares thus defined were systematically examined by tracking left to right and then right to left along adjoining rows. By examining different numbers of randomly selected images, it was shown that 400 micrographs is at least four times the number required to obtain repeatable, statistically significant values for pore diameter and total porosity. The Nucrel® microtruss pores were approximately circular in cross section (Fig. 1), and we defined the equivalent average pore diameter as the arithmetic mean of the diameters measured for 288,450 pores in 455 micrographs. For the appreciably distorted, i.e., noncircular, cross section (Fig. 1) Hytrel® pores, we defined an average equivalent diameter by approximating the pore area as circular, i.e., $d_e = [4A/\pi]^{0.5}$. The area $A$ was the arithmetic mean measured for 167,937 pores in 480 micrographs. As discussed below, more explicit accounting for Hytrel® pore shape may explain the intrinsic pore diffusion coefficients deduced for this truss. SEM images of edges exposed by microtoming (Fig. 1) show that the pores run "straight-through" and normal to the truss faces.

## Experimental Apparatus and Performance Validation

The apparatus (Fig. 2) measures rates and extents of surface cooling by liquid evaporation through porous coverings under conditions that are practically relevant. The experiments are sufficiently controlled to allow good closure of heat balances for equipment this small ($\pm 12\%$), deduction of quantitative data including intrinsic pore diffusion coefficients, and differentiation of heat transfer mechanisms, i.e., conduction and nonboiling evaporation. The evaporation chamber was a 33.0 mm outside diameter $\times$33.0 mm deep aluminum cylinder with a 3 mm thick flat

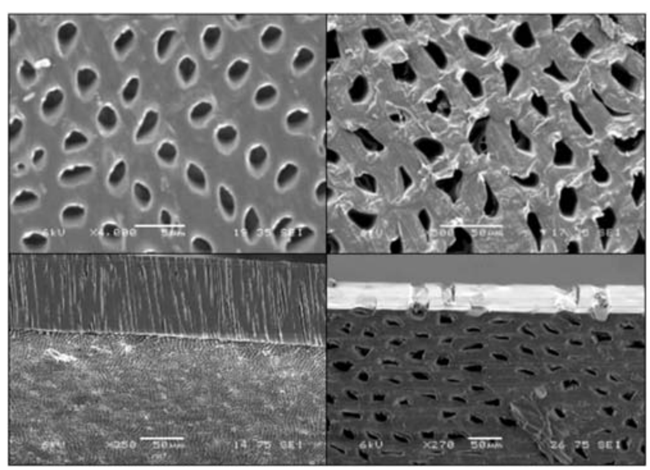

Fig. 1 SEMs of microtruss simulant surfaces (top panels) and edges exposed by microtoming (bottom panels). Left hand side panels: Nucrel®; right hand side panels: Hytrel®. Magnifications: top left panel, 4000×; top right panel, 500×.

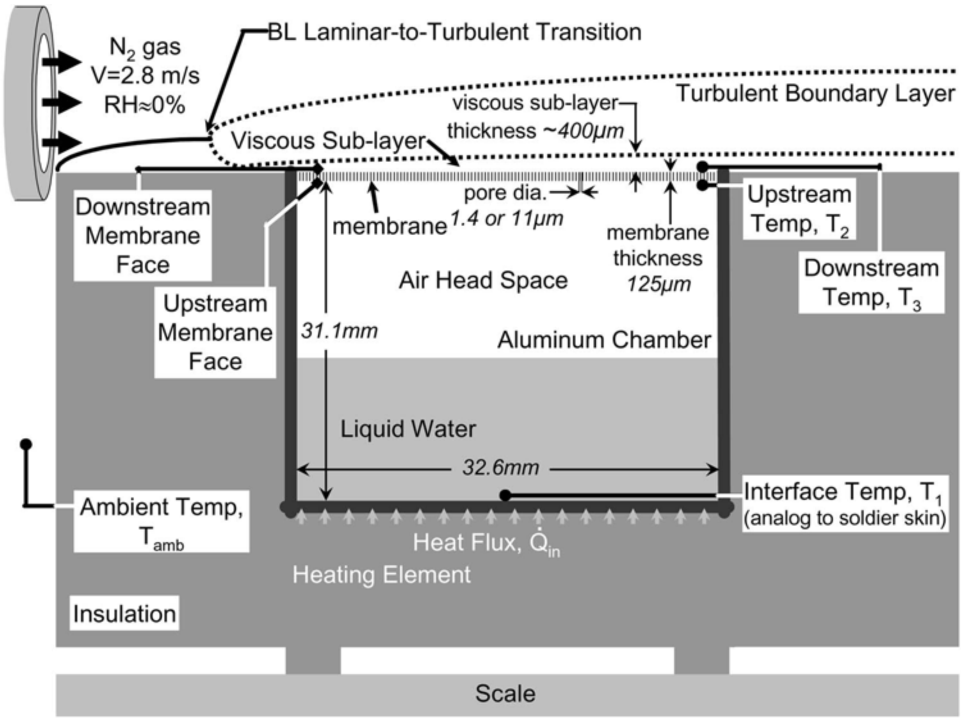


**Fig. 2 Schematic (not to scale) of apparatus for quantitative study of evaporative cooling of surfaces by modulation of latent heat carrier flow using barrier materials with microtruss and nanotruss architectures. Dotted BLs represent an average location because turbulence agitates the fluid boundaries.**

bottom—the evaporation surface. The outside wall of the cylinder was thermally insulated with a packing foam and a Styrofoam collar. The chamber was continuously weighed using a Mettler-Toledo 8001 series electronic balance (stated sensitivity of ±0.1 g). The temperatures of the evaporation surface ($T_1$) and the entrance (upstream, $T_2$) and exit (downstream, $T_3$) faces of the barrier material were each measured using Omega 5SC-TT-T-40-36 $T$-type thermocouples (0.076 mm bead outside diameter) connected to Omega HH2001LTC thermocouple readers. A continuous flow of dry nitrogen gas at 30°C temperature was directed over the top of the apparatus (Fig. 2) from a tube at an average exit velocity of $2.8 \pm 0.25$ m/s (measured using a VWR Enviro-Meter digital anemometer) to match the sweep gas rate of the ASTM upright cup method for determining vapor transmission rates through textiles [30]. The bottom face of the aluminum surface was heated by direct contact with an 85.55 mm outside diameter ProvoCraft® Candlsense™ electrical hot plate (stated maximum heat flux density of 3600 $W_t/m^2$).

In a typical experiment, $T_1$, $T_2$, and $T_3$ (Fig. 2) and the weight of liquid in the chamber were measured at approximately 2 min intervals for a known input heat load. Thermocouple $T_1$ was soldered to the center of the inside bottom wall of the evaporation chamber with generic rosin core (electrical) solder to provide good thermal contact. The beads of thermocouples $T_2$ and $T_3$ were attached to the upstream and downstream faces of the microtruss with a high-thermal-conductivity epoxy cement, OmegaBond® 101. Calibration experiments [31] showed that this method of bonding a tiny metal thermocouple sensor to soft (polymeric) materials gives reliable steady-state temperature measurements. All three thermocouples were approximately 14 mm from the chamber inside wall. We performed four negative control runs by capping the chamber with a nonporous latex membrane, four positive control runs (maximum water vapor transport rates) by leaving the chamber uncapped, and two runs each with replicate samples of the Nucrel® and Hytrel® microtruss.

Water vapor mass concentrations at the entrance and exit faces of the barriers were calculated from corresponding truss surface temperatures using the ideal gas law, the literature data on the saturation pressure of steam [32], and the assumption of 100% relative humidity (RH) and 0% *absolute* humidity (AH), respectively at the upstream and downstream faces of the barrier. The RH of the sweep gas at the nozzle exit measured with a Kestrel 4000 portable data-logging weather station (stated accuracy ±3.0% RH with a specified range of 5.0–95.0% RH) was 1.4–4.6%, which justifies the assumption of 0% AH owing to the very low water vapor content in the sweep gas. The assumption of a 100% RH at the upstream face of the microtruss simulant is reasonable because $T_2$ was intentionally kept below the temperature of the liquid water-air interface (i.e., the evaporation front). Consequently, some condensation of liquid water was observed on the entrance face of the polymer barrier. The inside walls of the evaporation chamber between the evaporation front and the microtruss entrance were kept above the temperature of the liquid water-air interface to prevent liquid water from condensing prematurely. Table 1 summarizes experimental conditions for runs with the various barrier materials.

A transient heat balance on the entire apparatus gives

$$\frac{d(C_pMT_1)}{dt} = \dot{Q}_{\text{in}} - Ah(T_1 - T_{\text{amb}}) - \dot{m}\Delta H_{fg}^{H_2O} \tag{1}$$

The overall thermal mass of the apparatus, $C_pM$, was obtained from the slope of the early stage heat-up curve (Fig. 3) for closed chamber (latex membrane) runs where evaporative transport is prevented ($\dot{m}=0$), and it is a reasonable approximation to neglect convective cooling owing to the relatively low values of $T_1 - T_{\text{amb}}$. Using this $C_pM$ value, the overall convective heat transfer coefficient $h$ was determined by fitting a lumped Newtonian cooling model to the cool-down curve for closed chamber runs (Fig. 3), recognizing that $\dot{Q}_{\text{in}}=0$ (heater off). The resulting $h$

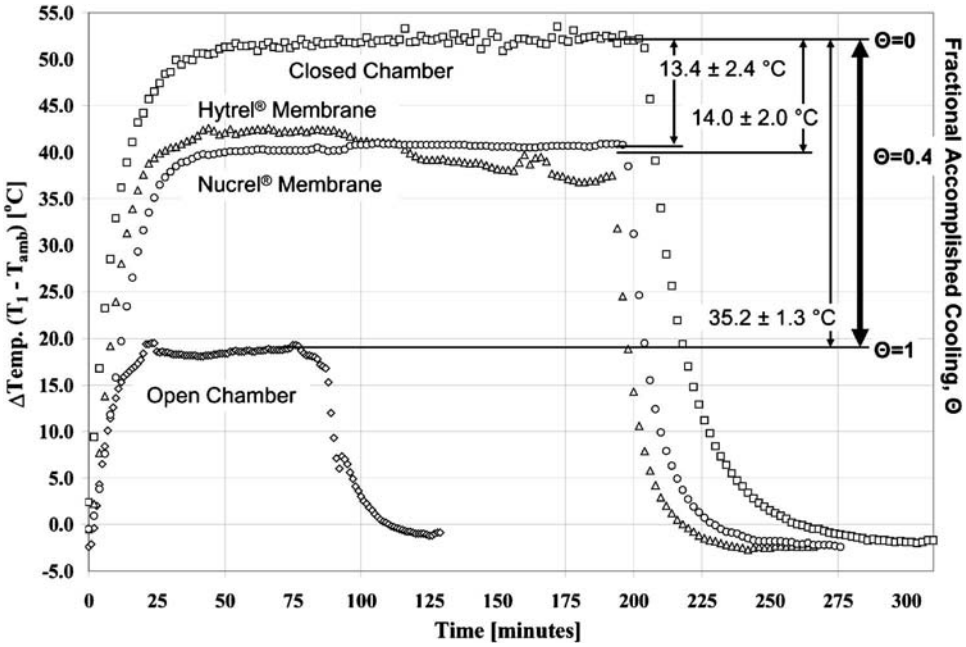


**Fig. 3 Typical temperature-time histories (corrected for ambient temperature) for evaporative cooling of an aluminum surface using a closed chamber (negative control), an open chamber (positive control), or microtruss simulant materials. The absolute latent and fractional accomplished cooling (defined in the text) are also shown.**

($192 \pm 25$ W/m$^2$ K) and $C_pM$ ($131 \pm 19$ J/K) determinations showed good repeatability for the four closed chamber runs. The mean $h$ value was within a typical range for forced convective heat transfer with air, i.e., 30–300 W/m$^2$ K [33], and the mean $C_pM$ result was within 15% of a value estimated from known masses and tabulated heat capacities of apparatus components [34]. Using these experimentally derived parameters in a steady-state, closed chamber heat balance (i.e., $d(MT_1)/dt=0$ and $\dot{m}\Delta H_{fg}^{H_2O}=0$ in Eq. (1)), the first two terms on the right hand side of Eq. (1) accounted for all thermal flows within +8.6% to −0.2%. For a steady-state heat balance with these $C_pM$ and $h$ values for the barrier runs (latent heat transfer from the chamber enabled), the three terms on the right hand side of Eq. (1) accounted for all thermal flows within +12.4% to +3.3%. These heat balance closures are good considering the small apparatus size and the use of lumped thermal physical parameters derived from transient heat-up and cool-down stages of the experiments.

Thermal buoyancy in the liquid water, conduction through the liquid water, and conduction along the aluminum walls were calculated to respectively account for 69.3%, 3.8%, and 26.7% of the axial heat flow in the evaporation chamber. Neglecting radial heat transfer, this implies that up to 73% of the heat input flowed through the water and, in principle, could have escaped the chamber via the latent heat carrier. In the present experiments, the maximum net latent heat transfer *from the chamber*, which occurred with an open, i.e., uncapped chamber, was 37.7% of the total heat input.

## Procedure for Evaporative Cooling Experiments

To thermally equilibrate it with ambient temperature, deionized water was stored overnight in a covered graduated cylinder on the laboratory bench. The evaporation chamber was weighed, charged to a depth of about 11 mm with equilibrated water (~7 gm), and then reweighed to more precisely determine the water weight by difference. The top of the evaporation chamber was then completely covered with a barrier material sealed taut by folding it over and binding its edges to the chamber outside the wall with an elastic band. Positive control runs (open chamber) omitted the barrier. The insulation collar was then placed around the chamber, and the chamber bottom was placed on the heater plate. A continuous flow of 30°C dry nitrogen gas was directed over the top of the apparatus (Fig. 2) from a tube at a linear velocity of $2.8 \pm 0.25$ m/s, measured at that temperature. The chamber bottom was then heated at $1350 \pm 20$ W$_t$/m$^2$ by manually adjusting a 110 V input variable transformer (Variac™) to a predetermined point. The chamber weight and temperatures of the chamber bottom and the membrane sample entrance and exit faces, $T_1$, $T_2$, and $T_3$, respectively, (Fig. 2) were each measured at 2 min intervals. Upon reaching steady state, these measurements were continued for approximately 150 min at the stated constant heat input. Steady state was defined as the condition in which measured values of $T_1$ and the rates of water removal from the chamber (the slopes of the curves in Fig. 4) were constant to within ±10%. Temperature-time histories of the aluminum surface throughout cool-down (Fig. 3), initiated by turning off the heater, were measured in all runs, providing data on evaporative cooling under transient conditions (not analyzed in this paper).

## Experimental Results

Figure 3 displays typical temperature-time histories for the Hytrel® and Nucrel® microtruss simulants and the closed chamber and open chamber control runs. To compare the evaporative cooling potency of different materials, Fig. 3 shows the absolute cooling owing to the latent heat transfer in °C and a corresponding nondimensional, fractional accomplished cooling $\Theta_a$ defined in Eq. (3). To correct for variations in room temperature from run to run, absolute latent cooling was defined as the difference, for the negative control, between the average steady-state temperature of the aluminum surface, $T_1$ (the plateau in Fig. 3), and room temperature $T_{amb}$ (measured at the beginning of the steady-state period), less this same difference when water vapor can exit the chamber through an overlaid membrane sample,

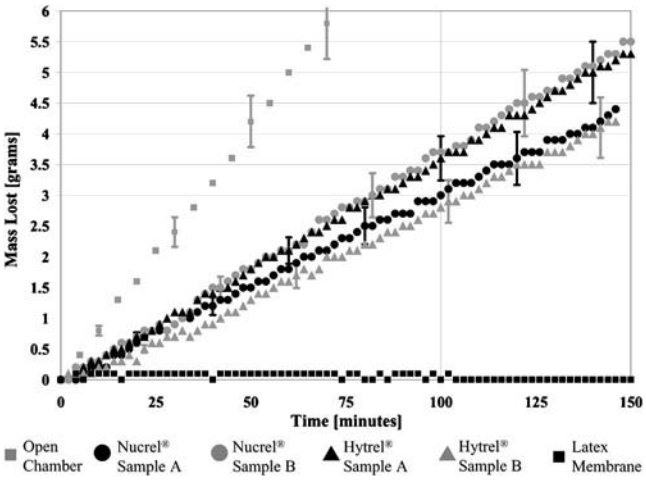


**Fig. 4 Cumulative mass of water vapor transported from the evaporation chamber as affected by time. The instantaneous flux of coolant vapor through the microtruss simulant pores is obtained from the first derivative of the curves shown.**

$$\text{Absolute latent cooling} = (T_{1,\text{closed}} - T_{\text{amb,closed}}) - (T_{1,\text{membrane}} - T_{\text{amb,membrane}}) \quad (2)$$

We defined $\Theta_a$ as the ratio of the absolute cooling with a truss on the chamber to the maximum evaporative cooling at the same heater power with the chamber uncovered,

$$\Theta_a = \frac{(T_{1,\text{closed}} - T_{\text{amb,closed}}) - (T_{1,\text{membrane}} - T_{\text{amb,membrane}})}{(T_{1,\text{closed}} - T_{\text{amb,closed}}) - (T_{1,\text{open}} - T_{\text{amb,open}})} \quad (3)$$

Thus, evaporative cooling approaches its maximum as $\Theta_a$ approaches unity, and a small $\Theta_a$ implies vapor transport limitations that strongly curtail latent heat removal from the chamber. Table 2 summarizes the average absolute cooling and corresponding $\Theta_a$'s and steady-state temperatures deduced for the 12 runs. The Nucrel® and Hytrel® microtruss simulants respectively resulted in $14.0 \pm 2.0°\text{C}$ and $13.4 \pm 2.4°\text{C}$ absolute latent cooling of the aluminum surface, corresponding to $\Theta_a$ values of about 0.4, i.e., a substantial fraction of the maximum possible evaporative cooling.

Figure 4 shows cumulative weight loss of the evaporation chamber, i.e., the aggregate weight of water evaporated from the aluminum surface from the time its temperature first attained steady state to time specified on the abscissa. The derivative of each curve at any time denotes the instantaneous steady-state rate of water mass transfer from the chamber at that time. Each curve is essentially linear over the steady-state period, implying that the corresponding mass flux of water vapor was constant. Accordingly, we defined the average rate of water vapor mass transfer from the apparatus $\dot{m}_{\text{av}}$ as the quotient of the cumulative steady-state weight loss and the cumulative time over which that weight loss occurred, i.e., as the average slopes of the curves in Fig. 4. Table 1 presents the measured $\dot{m}_{\text{av}}$ values for each microtruss simulant run and the average value for the four positive control runs. The uncertainty in $\dot{m}_{\text{av}}$ ($\pm 1.72 \times 10^{-8}$ kg/s, Table 1) was estimated by propagating the experimental uncertainties in the weight measurement $\pm 0.1$ g (in $\sim 5$ g) owing to the sensitivity of the balance and $\pm 0.1$ g owing to the drift of 0.1 g in the balance zero over a typical 9000 s run time and $\pm 20$ s owing to the uncertainty in the time measurement over the $\sim 9000$ s period, and then multiplying the result by the largest measured value of $\dot{m}_{\text{av}}$ (about $6.0 \times 10^{-7}$ kg/s). The constancy of $\dot{m}_{\text{av}}$ and $T_1$ for 90 min shows that the continuous depletion of liquid water did not undermine the stability of the experiment, e.g., because of reduced thermal convection in the water as its depth decreased or of the buildup of water droplets at the microtruss entrance.

**Table 2 Steady state temperatures, fractional accomplished cooling, and absolute latent cooling for evaporative cooling of an aluminum surface using a closed chamber (negative control), an open chamber (positive control), or microtruss simulant materials**

| Membrane {Number of runs} | Av. $T_{\text{amb}}$ (°C) | Av. $T_1$ (°C) | Fractional accomplished cooling | Absolute latent cooling (°C) |
|---|---|---|---|---|
| Closed chamber {4} | $27.2 \pm 0.2$ | $80.1 \pm 0.7$ | 0.00 | N/A |
| Open chamber {4} | $26.9 \pm 0.2$ | $44.6 \pm 0.4$ | 1.00 | $35.2 \pm 1.3$ |
| Nucrel® {2} | $27.5 \pm 0.2$ | $66.4 \pm 1.0$ | $0.40 \pm 0.06$ | $14.0 \pm 2.0$ |
| Hytrel® {2} | $27.5 \pm 0.2$ | $67.0 \pm 1.4$ | $0.38 \pm 0.07$ | $13.4 \pm 2.4$ |

## Mathematical Modeling

Intrinsic coefficients for pore diffusion of water vapor can be deduced from the present measurements (Fig. 4) by using a mathematical model to decouple the appreciable ($\sim 50\%$) contributions of the boundary layers (BLs) to the overall rate of water vapor mass transfer from the chamber and by determining the contributions of Stefan flow (convection caused by diffusion) and Knudsen flow (molecule-wall versus molecule-molecule collisions) to pore transport. Calculations show that Stefan flow contributes less than 13.0% enhancement, and this transport mode was ignored. For pores of circular cross section, Knudsen effects can be estimated from an engineering correlation relating the Knudsen impacted diffusion coefficient $D_{\text{eff}}$ for a pore of radius $r_e$ (here in meters) to the coefficient for diffusion in a continuum fluid ($\text{Kn} < 0.01$), $D$ [34],

$$\frac{1}{D_{\text{eff}}} = \frac{\tau}{\varepsilon_v}\left(\frac{1}{D} + \frac{1}{97 r_e \sqrt{T/m}}\right) \quad (4)$$

Here, $T$ is in Kelvins, $m$ is in g/(g mole), and the dimensionless tortuosity $\tau$ is an adjustable parameter to account for variability in pore axis orientation and pore cross sectional area [35]. Our SEM measurements found that the Nucrel® pores have approximately uniform circular cross sections and run straight through the microtruss with their axis essentially normal to the truss face (Fig. 1), making $\tau = 1$ a reasonable approximation. Using this value and porosities ($\varepsilon_v$) from Table 1, Eq. (4) predicts that $D_{\text{eff}}$ should be 10.5% less than $D$ for Nucrel®. The Hytrel® pores also run straight through, but have noncircular cross sections with considerable variability in width from pore to pore (Fig. 1). Thus, without detailed information on the tortuosity of these pores, the quantitative applicability of Eq. (4) for the Hytrel® is suspect. Nevertheless, to allow a qualitative comparison with Nucrel®, we approximated the Hytrel® pores as circular in cross section and $\tau$ as 1. Using $\varepsilon_v$ from Table 1, Eq. (4) then predicts that Knudsen effects reduce $D_{\text{eff}}$, about 1.3% below $D$ for the Hytrel® pores.

To assess the apparatus performance and determine the intrinsic coefficient for diffusion of dilute water vapor (10.4 mole %) in air at about 1 atm total pressure in the microtruss pores, we derived (Appendix) and solved a predictive mathematical model for the rates of water vapor mass transfer $\dot{m}_{\text{av}}$ from the apparatus of Fig. 1,

$$\dot{m}_{\text{av}} = \int_{r_o}^{r=0} \frac{2\pi r}{R_{\text{BL,downstream}} + R_{\text{mem}}} \left\{ \int_{r_o}^{r=0} \frac{1}{\delta(r) v(r)} \left[ \frac{\rho_{\text{chamber}} - \rho(r)}{R_{\text{BL,upstream}}} - \frac{\rho(r)}{R_{\text{mem}} + R_{\text{BL,downstream}}} \right] dr - \rho_{\text{ambient}} \right\} dr \quad (5)$$

Equation (5) was developed by modeling effects of (1) BL mass transfer and radial gradients of water vapor concentration at the

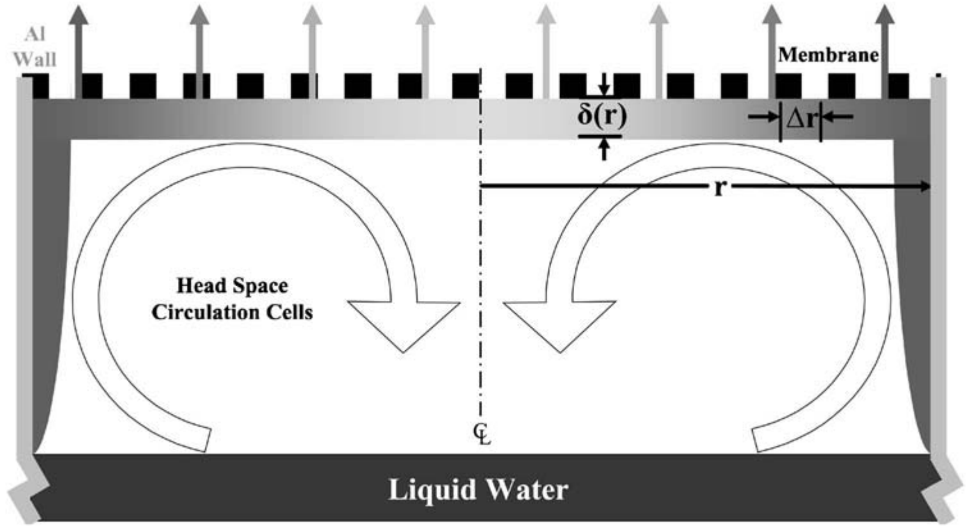


**Fig. 5 Schematic cross section of the evaporation chamber to illustrate chirality of the thermal buoyancy driven flows and the radial concentration gradient across the upstream face of the microtruss**

microtruss entrance (impacting $R_{\mathrm{BL,upstream}}$ and $\rho(r)$) and (2) BL mass transfer at the truss exit (impacting $R_{\mathrm{BL,downstream}}$). At the truss exit, the flow of dry nitrogen creates low AH, so $\rho_{\mathrm{ambient}} \approx 0$ for all $r$. The mass transfer resistance of the microtruss itself, $R_{\mathrm{mem}}$, is obtained from

$$R_{\mathrm{mem}} = \frac{L}{\varepsilon_v D_{\mathrm{eff}}} \tag{6}$$

if $D_{\mathrm{eff}}$ is known, e.g., from the literature. Alternatively, Eq. (5) can be solved for $R_{\mathrm{mem}}$ using experimental values of $\dot{m}_{\mathrm{av}}$, and $D_{\mathrm{eff}}$ can then be obtained from Eq. (6). Both approaches were used here.

Tracer measurements found that thermal-buoyancy-induced convection in the chamber headspace caused a radial inward flow of water vapor-air mixture. This creates a BL along the microtruss entrance face, from which diffusion of water vapor through the microtruss pores to the ambient (Fig. 5) causes a radial water vapor concentration gradient at the microtruss entrance. Mass continuity for a fluid element adjacent the microtruss gives

$$\frac{d\rho(r)}{dr} = \frac{1}{\delta(r)v(r)}\left[\frac{\rho_{\mathrm{chamber}} - \rho(r)}{R_{\mathrm{BL,upstream}}} - \frac{\rho(r) - \rho_{\mathrm{ambient}}}{R_{\mathrm{mem}} + R_{\mathrm{BL,downstream}}}\right] \tag{7}$$

The boundary condition for Eq. (7) is the mass concentration of water vapor at the evaporation chamber wall ($r=r_o$), which is obtained from the temperature of the microtruss entrance face ($T_2$), the ideal gas law, and the properties of steam assuming saturation. The radial inward velocity of the air-water vapor mixture across the microtruss at the chamber wall was calculated from a correlation in Deen [36] and was within about a factor of 2 of experimental values of this velocity we obtained from tracer studies.

Tracer studies also revealed a laminar-to-turbulent transition in the downstream BL ahead of the leading edge of the microtruss face. However, the Reynolds number based on plate length at this location was only about 12,000, which is far below the 300,000 threshold for the transition to turbulence expected for flat plate flow. We believe that the observed turbulent flow is caused by surface roughness. The "beads" on the Styrofoam collar protruded about 1 mm above the collar surface in a roughly hexagonal pattern, a substantial incursion into the roughly 3 mm thick laminar sublayer (as calculated from Blasius' solution for flow over a flat plate). Since the membrane sample itself was smooth, $R_{\mathrm{BL,downstream}}$ was estimated from a correlation of the Sherwood number for turbulent flow over a smooth horizontal flat plate [34]. However, the use of the resulting $R_{\mathrm{BL,downstream}}$ values in Eq. (5) badly underestimated the observed $\dot{m}_{\mathrm{av}}$ values, leading us to conclude that either the correlation considerably overestimated $R_{\mathrm{BL,downstream}}$ or $R_{\mathrm{BL,downstream}}$ was determined by the mass transfer resistance of the viscous sublayer beneath the turbulent BL. We assumed the latter and thus that the concentration envelope where $\rho(r)$ first decreases to $\sim 0$ is the outer edge of the viscous sublayer. The thickness of this sublayer was estimated using Prandtl's "law of the wall" [37],

$$u^+(x) = \frac{U}{u_\tau(x)} = \frac{\delta(x)u_\tau(x)}{\nu} = y^+(x) \tag{8}$$

The exit faces of the microtrusses were very smooth compared to the surface of the Styrofoam collar. Thus, the friction velocity $u_\tau(x)$ was determined from the sheer stress on the wall using a correlation for skin friction from turbulent flow over a *smooth* surface [38] that accounts for the presence of a viscous sublayer

$$u_\tau(x) = U\left(\frac{0.0592\,\mathrm{Re}_x^{-1/5}}{\rho}\right)^{1/2} \tag{9}$$

This correlation is valid for $10^5 < \mathrm{Re}_x < 10^7$ but was used here for $\mathrm{Re}_x = 1.2 \times 10^4$. To find the average thickness of the viscous sublayer over the barrier, we averaged $\delta(x)$ from Eq. (8) over the sample diameter using Eq. (9) for $u_\tau(x)$ and the fact that the dimensionless thickness of the viscous sublayer $y^+$ is roughly 5 [37],

$$\bar{\delta} = \frac{1}{2r_o}\int_0^{2r_o} \frac{5\nu}{U(0.0592\,\mathrm{Re}_x^{-1/5}/\rho)^{1/2}}dx \tag{10}$$

Dividing the resulting average viscous sublayer height by the diffusion coefficient of water vapor in nitrogen gives the mass transfer resistance for the downstream BL:

$$R_{\mathrm{BL,downstream}} = \frac{\bar{\delta}}{D_{\mathrm{H_2O,nitrogen}}} \tag{11}$$

Using values of $R_{\mathrm{BL,downstream}}$ from Eq. (11), we solved Eq. (5) numerically for $\dot{m}_{\mathrm{av}}$. Values of $\rho(r)$ were calculated by numerically integrating Eq. (7) using measured values of $T_2$ and values of $R_{\mathrm{mem}}$ calculated from Eq. (6) using literature data for $D_{\mathrm{H_2O,air}}$ [34]. Figure 6 shows that the $\dot{m}_{\mathrm{av}}$ predictions became increasingly close to the experimental data, as the model was steadily improved to more realistically capture the mass transport details of

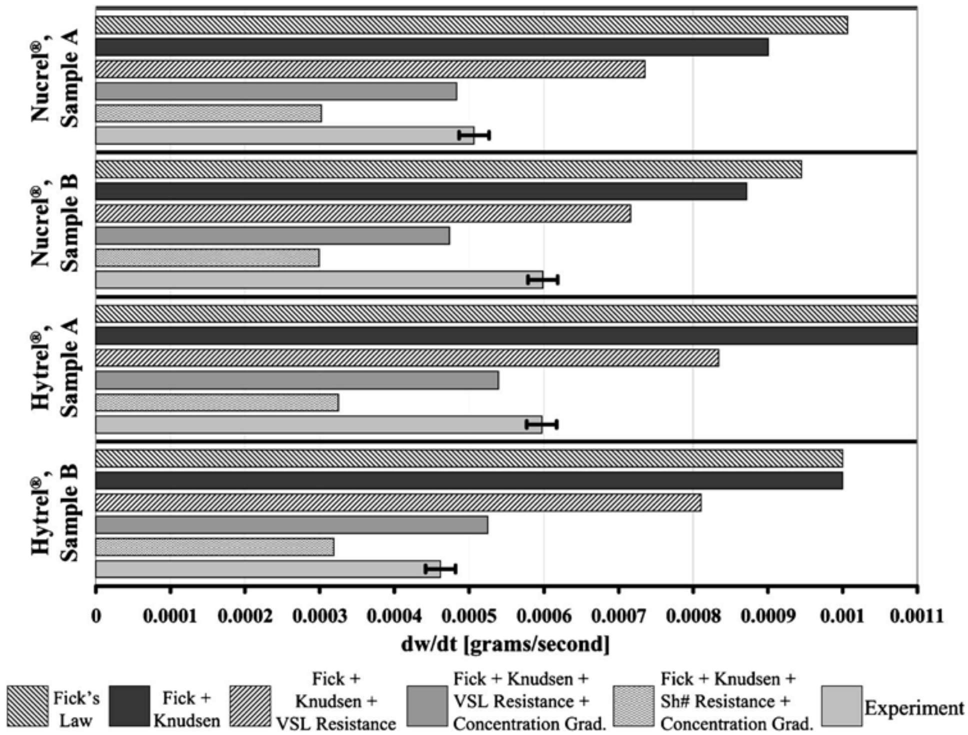


**Fig. 6 Comparison of experimental (light gray) rates of water vapor mass transport from the evaporation chamber for the four experiments with microtruss stimulant barriers, with rates predicted by increasingly refined mass transfer models (various fills)**

the apparatus of Fig. 1, i.e., from simple 1D continuum diffusion to correcting for (1) slight rarefaction (Knudsen effects) on the pore diffusion coefficient, (2) radial gradients in water vapor concentration at the microtruss entrance, (3) upstream BL mass transfer resistance, and (4) downstream BL mass transfer resistance. The inclusion of all four refinements gave $\dot{m}_{av}$ predictions that agree with experiment to within +14% to −21%, building confidence in the reliability of the apparatus and in the physical assumptions of the modeling.

To compare the latent heat transmission capabilities of different microtruss simulants on a consistent basis, and thus provide a reliable foundation for engineering design, we deduced an intrinsic, i.e., apparatus-independent, pore diffusion coefficient $D_{eff}$ for (dilute) water vapor in atmospheric pressure air for each truss sample. The approach was to numerically solve Eqs. (5) and (7) simultaneously for $\rho(r)$ and $R_{mem}$ using MATLAB. The resulting $R_{mem}$ values were then used in Eq. (6) to calculate $D_{eff}$. The results (Table 3) agree to within 35% of the experimental bulk diffusion value, $2.59\times10^{-5}$ m$^2$/s, reported by Deen [36], for continuum regime diffusion of water vapor in molecular nitrogen ($N_2$) at 308 K.

## Discussion

Despite low total porosity (<12%, Table 1), barrier materials with microtruss architectures (Fig. 1) provide substantial evaporative cooling of strongly heated surfaces (Fig. 3, Table 2) by transport of latent heat-carrying vapor through the truss voids. Up to 25% of input heat energy was carried away by latent heat transfer through porous membranes, and the ratio of conductive to latent heat transport across the porous membranes ranged between 3:1 and 5:1. Water vaporization and transport through two different polymer sheets with microtruss features cooled a surface heated at ~1.4 kW/m$^2$ by about 13°C, about 40% of the maximum evaporative cooling attainable with water for the same heat load with the evaporation chamber uncapped (Table 2, Fig. 3). Because microtruss architectures show promise to provide high mechanical strength, light weight, and breatheability in soft materials, docu-

**Table 3 Comparison of intrinsic (i.e., apparatus-independent) coefficients for diffusion of dilute water vapor in air (total pressure, 1 atm) through the microtruss pores with values predicted for mutual diffusion of water vapor in air for continuum conditions and with correction for the onset of fluid rarefaction (Eq. (4) in the text)**

| Overlay | Knudsen number | Rarified theory $D_{H_2O,air}$ (m$^2$/s) | Apparatus-independent experimental $D_{eff}$ (m$^2$/s) | % Difference rarified versus experiment (%) |
|---|---|---|---|---|
| Nucrel®, Sample A | 0.099 | 2.12*E*−05 | 1.95*E*−05 | −9 |
| Nucrel®, Sample B | 0.071 | 2.18*E*−05 | 2.68*E*−05 | 19 |
| Hytrel®, Sample A | 0.007 | 2.33*E*−05 | 1.68*E*−05 | −38 |
| Hytrel®, Sample B | 0.008 | 2.36*E*−05 | 1.68*E*−05 | −40 |

mentation of latent heat flux densities this high under practically realistic conditions supports the idea that microtruss materials can protect humans and inanimate objects from mechanical and thermal damage simultaneously.

Further assessing this proposition requires latent heat transmission information unencumbered by the idiosyncrasies of apparatus or experimental conditions. BLs at the microtruss entrance and exit accounted for roughly half of the total resistance to cooling vapor mass transfer from the present evaporation chamber (Fig. 2). Mathematical modeling (described above) allowed the apparatus-independent mass transfer resistance for the microtruss, $R_{\text{mem}}=L/[D_{\text{eff}}\varepsilon_v]$ and the intrinsic diffusion coefficient $D_{\text{eff}}$ to be disaggregated from the measured rates of water vapor transport from the chamber. The resulting $D_{\text{eff}}$ values (Table 3) for the Nucrel® and Hytrel® microtruss simulants are in reasonable agreement with predictions for mutual diffusion of dilute water vapor in air in the continuum regime ($\text{Kn}<0.01$) and with literature values for mutual diffusion of dilute water vapor in $N_2$ gas under continuum conditions [36]. The differences in the experimentally derived $D_{\text{eff}}$ values for the two microtruss simulants are discussed below.

For engineering designs incorporating other microtrusses with straight-through pores, comparable pore widths and geometries, and known thickness, the present $D_{\text{eff}}$ values allow an initial estimate of the water vapor/air diffusion resistance in the truss pores. The *steady state* latent heat flux density through the microtruss can then be estimated for various operating conditions by formulating the total mass transfer resistance of the system as a series combination of the mass transfer resistances intrinsic for the truss itself and for the upstream and downstream BLs, then calculating $\dot{m}_{\text{av}}$ from Eq. (5), or its equivalent, for the particular evaporator, and then multiplying $\dot{m}_{\text{av}}$ by the average latent heat of vaporization of water for the temperature regime of interest.

To further benchmark the efficacy of the microtruss simulants for latent heat transmission, it is instructive to estimate what level of convective cooling would be needed to provide equivalent rates of heat removal from the surface. One approach is to assume a constant driving temperature gradient, $\Delta T$, for convection and to calculate the required magnitude of the heat transfer coefficient, $h_c$. Alternatively, one could assume a constant value for $h_c$ and calculate the required $\Delta T$. Here, we do the former by taking $\Delta T$ as the difference between the evaporation chamber surface temperature at steady state, $T_1$, and a reasonable lower temperature, $T_a$, i.e., temperature at standard conditions: 298.2 K. Two cases of interest are (1) the convective heat transfer coefficient $h_{c,\text{app}}$ corresponding to the rate of latent heat removal experimentally measured with the present apparatus and operating conditions, $\dot{Q}_{L,\text{app}}$ and (2) an upper bound convective heat transfer coefficient $h_{c,\text{mem}}$ corresponding to the idealized case of latent heat removal, $\dot{Q}_{L,\text{mem}}$, which would be possible at the same operating conditions if the only mass transfer resistance to water vapor removal from the chamber were the intrinsic resistance of the microtruss pores. Thus,

$$h_{c,\text{app}} = \frac{\dot{Q}_{L,\text{app}}}{A(T_1 - T_a)} \quad \text{and } h_{c,\text{mem}} = \frac{\dot{Q}_{L,\text{mem}}}{A(T_1 - T_a)} \qquad (12)$$

where $\dot{Q}_{L,\text{mem}}=\dot{m}_{\text{mem}}\Delta H_{\text{vap}}^{H_2O}$, $\dot{m}_{\text{mem}}=D_{\text{eff}}\varepsilon_v(\rho_i-\rho_o)/L$, and $\rho_o$ and $\rho_i$ for this case are respectively taken as zero and at the vapor pressure of water at $T_1$. The magnitudes of the resulting convective heat transfer coefficients (Table 4) are comparable to those typical of forced convection heat transfer with air near ambient temperatures (298.2 K) [33].

Assuming pores of circular cross section, Eq. (4) predicted that rarefaction (Knudsen) effects reduce the continuum regime diffusion coefficient for the Hytrel® and Nucrel® pores by 1.3% and 10.5%, respectively (Table 3) owing to the smaller average width and thus larger Kn of the Nucrel® (~1.2 $\mu$m, Kn ~ 0.1) versus the Hytrel® pores (~13 $\mu$m, Kn ~ 0.01). However, the $D_{\text{eff}}$ values derived for the Hytrel® pore from the experimental data were about 27% smaller than those for the Nucrel® pores (Table 3, column 5). A possible explanation is Knudsen-inhibited diffusion in the significant fraction of the Hytrel® pore volume that is not present in a circular cross section but rather in pinched down shapes that approximate narrow rectangles or isosceles triangles of small apex angle (Fig. 1). In qualitative support of this proposal, we calculated that if 40% of the Hytrel® pore volume was sufficiently distorted to reduce the continuum diffusion coefficient tenfold, then the $D_{\text{eff}}$ values derived from the Hytrel® measurements would be about 35% lower than those for Nucrel®. A more in-depth assessment of pore shape effects would require reliable measurements of the tortuosity of the Hytrel® pores and/or a large number of SEM measurements to quantify the distortions in pore cross section, ideally as affected by pore depth. Such studies are beyond the scope of the present work.

**Table 4 Apparent average and intrinsic convective heat transfer coefficients that would give rates of heat removal from surfaces equal to those obtained by NBEC (1) as measured with the present apparatus and (2) as would be possible if the only mass transfer resistance to water vapor removal from the evaporation chamber arose from the membrane pores. See Eq. (12) and accompanying narrative in the text.**

| Overlay | $(T_1-T_a)^a$ (K) | $h_{c,\text{app}}$ (w/m$^2$ K) | $h_{c,\text{mem}}$ (w/m$^2$ K) |
|---|---|---|---|
| Nucrel®, Sample A | 39.8 | 39 | 61 |
| Nucrel®, Sample B | 43.0 | 43 | 68 |
| Hytrel®, Sample A | 42.5 | 42 | 62 |
| Hytrel®, Sample B | 41.3 | 35 | 48 |

[a]Assumed driving force for thermal convection.

Despite differences in their pore width and geometry, we observed no significant difference in the fractional accomplished cooling $\Theta_a$ between Nucrel® and Hytrel® (Fig. 3, Table 2), putatively because (1) the effect of variations in intratruss mass transfer resistance is tempered by the sizable (~50% of the total) contribution from the upstream and downstream BLs; (2) the intrinsic diffusion coefficients for the two microtruss simulants are not that different ($1.7\times10^{-5}$ versus $2.7\times10^{-5}$ m$^2$/s in the worst case, Table 3); and (3) the $D_{\text{eff}}$ determinations reflect experimental uncertainty of ±6.6%.

The present apparatus and operating procedures are useful tools for a quantitative characterization of the latent heat transfer capabilities of various porous media including materials with microtruss architectures. The equipment provides steady state heat balance closures to within ±12% for practically realistic heat loads, temperatures, and working fluid (water). The method of continuously weighing the entire evaporation chamber requires some care, but enables direct measurement of the mass fluxes of latent heat carrier responsible for latent heat transmission. Moreover, intrinsic, i.e., free of apparatus artifacts, coefficients for the diffusion of latent heat carrier through the microtruss voids can be deduced from these mass fluxes by mathematical modeling to disaggregate BL and other mass transfer resistances dictated by the apparatus geometry and operating conditions. Design and operation to sustain thermal buoyancy in the coolant liquid and the coolant vapor headspace simplify this mathematical modeling.

## Conclusions

**Latent Heat Transfer.** Thin (~120 $\mu$m) sheets of soft materials with microtruss architectures, including pore widths of ~1–15 $\mu$m, enable substantial evaporative cooling of surfaces, *without boiling*. At appreciable surface heat flux densities (1.4 kW$_t$/m$^2$) and despite their low overall porosity (7.5–11.2%), the present microtruss structures provided evaporative cooling of

13–14°C (about 40% of the maximum attainable, i.e., with an uncovered evaporation chamber). The cooling mechanism is latent heat transfer enabled by diffusion of evaporated coolant through the microtruss voids (pores). Thus, the efficacy of microtrusses for evaporative cooling of a nearby surface can be quantified in terms of a pore diffusion coefficient, microtruss thickness, and coolant heat of vaporization. The present rates of latent heat lift can be benchmarked by estimating the equivalent thermal convection that would be needed to provide identical surface cooling rates. For example, equivalent convective heat transfer coefficients as high as 43 $W/m^2$ K, i.e., comparable to those typical of forced convective cooling with air, were calculated for the Nucrel® microtruss simulant by assuming a $\Delta T$ equal to the difference between the surface temperature and standard temperature (298.2 K).

**Pore Width and Shape.** Effects of width and shape of microtruss pores must be understood to interpret experimental observations and design reliable evaporative cooling systems. Here, apparent average pore width was varied from about 15 $\mu$m (Kn $\sim$0.01) to 1 $\mu$m (Kn$\sim$0.1), and no impact on measured cooling was observed. This result is consistent with small estimated effects of rarefaction in this range of Knudsen numbers (<10% reduction for the smaller pores), together with similar overall porosities and substantial ($\sim$50%) contributions from the BLs on either microtruss external face. However, intrinsic coefficients for mutual diffusion of dilute water vapor in air deduced for the microtruss pores exhibited a contrarian variation, i.e., smaller values for the pores of *larger* width. This may be caused by rarefaction-impeded diffusion owing to the distortion of pore cross section, considerably reducing the effective pore width. Further testing of this hypothesis by measurements of tortuosity and characterization of pore shapes and sections was beyond the scope of this work.

**Apparatus Performance and Utility.** The present apparatus design and operating procedures simultaneously quantify the latent heat transmission, thermal conduction, and coolant vapor mass transfer characteristics of materials with microtruss architectures under practical heat loads with good reliability. Heat balances close to within ±12% and intrinsic pore diffusion coefficients deduced from measured water vapor mass flow rates are in satisfying agreement with the literature. Thus, the present experimental approach and mathematical modeling show promise for quantifying pore mass transfer, latent heat transfer (evaporative cooling and condensation heating), and thermal conduction characteristics of other microtruss materials, and indeed other porous materials and media more generally, for diverse practical working fluids, surfaces, heat loads, and temperature differences.

**Applications.** Soft materials with microtruss (and nanotruss, i.e., pore widths of 10–1000 nm) architectures show promise for providing high mechanical strength and light weight in sheetlike structures. The present results support the proposition that microtrusses can simultaneously protect against mechanical and thermal damage. More generally, microtrusses have the potential to integrate mechanical protection, breathability and cooling in shapeable, and barrier materials to protect, inter alia, humans, microelectromechanical systems (MEMS), nanocomponents (e.g., electronics), and larger structures such as turbine blades and space vehicle heat shields. This paper provides latent heat and mass transfer data, pore diffusion coefficients, and mathematical modeling methods for the design, operation, and performance assessment of materials and devices that exploit microtruss architectures for thermal management, mechanical protection, vapor separations, and combinations thereof. One application is *nonboiling* evaporative cooling (NBEC), which is of interest when boiling temperatures at the prevailing pressure would be intolerable, e.g., cooling humans, sensitive electronics, biological specimens, archeological samples, etc. NBEC provides reasonably high heat flux densities at lower temperatures. Integration with microfluidic channel networks can enable controlled delivery of latent heat carriers to tiny or difficult-to-access components.

## Acknowledgment

This research was supported by the U.S. Army through the Institute for Soldier Nanotechnologies under Contract No. DAAD-19-02-D-0002 with the U.S. Army Research Office. The content does not necessarily reflect the position of the Government, and no official endorsement should be inferred. We thank Professor Ludovic Noels for valuable guidance on numerical modeling, Dr. Catherine Byrne for assistance in developing the experimental apparatus, Dr. Vahik Krikorian for expert guidance on SEM measurements and interpretation, and Dr. Vivek Kapur and Dr. Wayne Marsh of DuPont for supplying Hytrel® and Nucrel® sheets that we used as microtruss simulants. Hytrel® and Nucrel® are registered trademarks of the DuPont Company.

## Nomenclature

$A$ = area
$C_p$ = specific heat at constant pressure
$D$ = continuum diffusion coefficient
$d_e$ = equivalent diameter
$D_{\mathrm{eff}}$ = Knudsen impacted diffusion coefficient
$D_{\mathrm{H_2O,air}}$ = continuum diffusion coefficient of water vapor in air
$h$ = convection coefficient
$h_{c,\mathrm{app}}$ = experimentally measured latent heat transfer coefficient
$h_{c,\mathrm{mem}}$ = upper bound convective heat transfer coefficient
$M$ = mass
$m$ = molecular mass
$\dot{m}$ = mass transfer rate
$\dot{m}_{\mathrm{mem}}$ = intrinsic mass transfer rate across the microtruss
$\dot{m}_{\mathrm{av}}$ = average water vapor mass transfer rate from the apparatus
$\dot{Q}_{\mathrm{in}}$ = heat input
$\dot{Q}_{L,\mathrm{app}}$ = rate of latent heat removal experimentally measured with the apparatus
$\dot{Q}_{L,\mathrm{mem}}$ = idealized latent heat removal rate for the microtruss only
$r$ = radial coordinate
$R_{\mathrm{BL,downstream}}$ = downstream membrane mass transport resistance owing to a BL
$R_{\mathrm{BL,upstream}}$ = upstream membrane mass transport resistance owing to a BL
$\mathrm{Re}_x$ = Reynolds number at coordinate $x$ along a flat plate
$R_{\mathrm{mem}}$ = mass transport resistance of the membrane
$r_o$ = outer radius of the evaporation chamber
$T$ = temperature
$T_1$ = evaporation chamber bottom surface temperature
$T_2$ = upstream membrane surface temperature
$T_3$ = downstream membrane surface temperature
$T_a$ = temperature at standard conditions (298.2 K, 1 atm)
$T_{\mathrm{amb}}$ = ambient temperature
$U$ = free stream velocity
$u^+(x)$ = dimensionless velocity
$u_\tau$ = friction velocity
$v(r)$ = velocity
$W_t$ = watts, thermal
$y^+(x)$ = dimensionless BL thickness
$\delta$ ($x$ or $r$) = BL thickness at coordinate $x$ or $r$

$\bar{\delta}$ = average viscous sublayer thickness
$\Delta H_{fg}^{H_2O}$ = latent heat of vaporization
$\Delta T$ = driving temperature gradient
$\varepsilon_v$ = void fraction (porosity)
$\Theta_a$ = fractional accomplished cooling
$\nu$ = kinematic viscosity
$\rho(r)$ = mass concentration
$\rho_{\text{ambient}}$ = mass concentration in the ambient environment
$\rho_{\text{chamber}}$ = mass concentration in the evaporation chamber
$\tau$ = tortuosity

## Appendix

Here, we derive Eqs. (5) and (7) from a mass continuity balance on a fluid element in the vicinity of the upstream microtruss face (Fig. 5). The element is a cylindrical shell of radius $r$, width $\Delta r$, and height $\delta(r)$, approximated as the BL thickness. The top surface of the element is the upstream truss face, and the element follows the fluid flow from the outer radius of the evaporation chamber, $r_o$, toward the chamber center, $r=0$ through incremental reductions in its radius by $\Delta r$ (Fig. 5). By mass continuity, the water vapor contained within the element must equal the mass entering minus the mass leaving the element,

$$\frac{d\rho(r)}{dt}dA(r)\delta(r) = \frac{dm_{\text{in}}}{dt} - \frac{dm_{\text{out}}}{dt} \tag{13}$$

By expanding the left hand side of Eq. (13) in a Taylor series and canceling like terms,

$$\frac{d\rho(r)}{dr}\Delta r dA(r)\delta(r) = \frac{dm_{\text{in}}}{dt}\Delta t - \frac{dm_{\text{out}}}{dt}\Delta t \tag{14}$$

To put the fluid element in a Lagrangian reference frame, a substitution is made for $\Delta t$ to give

$$\frac{d\rho(r)}{dr}\Delta r dA(r)\delta(r) = \frac{dm_{\text{in}}}{dt}\frac{\Delta r}{v(r)} - \frac{dm_{\text{out}}}{dt}\frac{\Delta r}{v(r)} \tag{15}$$

Recognizing that the mass flows in and out of the fluid element are governed respectively by diffusion (in) through the BL on the upstream barrier face and diffusion (out) through the barrier and downstream BL, the following substitutions are made:

$$\frac{dm_{\text{in}}}{dt} = \frac{\rho_{\text{chamber}} - \rho(r)}{R_{BL,\text{upstream}}}dA(r) \quad \text{and}$$

$$\frac{dm_{\text{out}}}{dt} = \frac{\rho(r) - \rho_{\text{ambient}}}{R_{\text{mem}} + R_{BL,\text{downstream}}}dA(r) \tag{16}$$

where $\rho_{\text{amblent}} \approx 0$ due to a cross flow of dry nitrogen. Finally, substituting the expressions of Eq. (16) into Eq. (15) and canceling like terms, the desired result Eq. (7) is obtained,

$$\frac{d\rho(r)}{dr} = \frac{1}{\delta(r)v(r)}\left[\frac{\rho_{\text{chamber}} - \rho(r)}{R_{BL,\text{upstream}}} - \frac{\rho(r) - \rho_{\text{ambient}}}{R_{\text{mem}} + R_{BL,\text{downstream}}}\right] \tag{7'}$$

Both BL resistances are calculated in the main text, and Eq. (7) is combined with Eq. (17), an integral representation of Fick's law for diffusion, to create the complete apparatus transport model (Eq. (5)),

$$\dot{m}_{\text{av}} = \int_{r_o}^{r=0} \frac{2\pi r}{R_{BL,\text{downstream}} + R_{\text{membrane}}}[\rho(r) - \rho_{\text{ambient}}]dr \tag{17}$$

$$\dot{m}_{\text{av}} = \int_{r_o}^{r=0} \frac{2\pi r}{R_{BL,\text{downstream}} + R_{\text{mem}}}\left\{\int_{r_o}^{r=0} \frac{1}{\delta(r)v(r)} \times \left[\frac{\rho_{\text{chamber}} - \rho(r)}{R_{BL,\text{upstream}}} - \frac{\rho(r)}{R_{\text{mem}} + R_{BL,\text{downstream}}}\right]dr - \rho_{\text{ambient}}\right\}dr \tag{5'}$$

which was solved numerically via MATLAB for the unique combination of $R_{\text{mem}}$ and $\rho(r)$ that satisfies the boundary condition.

## References


[1] Jang, J.-H., Ullal, C. K., Choi, T. Y., LeMieux, M. C., Tsukruk, V. V., and Thomas, E. L., 2006, "3D Polymer Microframes That Exploit Length-Scale-Dependent Mechanical Behavior," Adv. Mater. (Weinheim, Ger.), **18**(16), pp. 2123–2127.
[2] Choi, T., Jang, J.-H., Ullal, C. K., LeMieux, M. C., Tsukruk, V. V., and Thomas, E. L., 2006, "The Elastic Properties and Plastic Behavior of Two-Dimensional Polymer Structures Fabricated by Laser Interference Lithography," Adv. Funct. Mater., **16**, pp. 1324–1330.
[3] Karniadakis, G., and Beskök, A., 2002, *Micro Flows: Fundamentals and Simulation*, Springer, New York.
[4] de Gennes, P., Brochard-Wyart, F., and Quere, D., 2004, *Capillarity and Wetting Phenomena: Drops, Bubbles, Pearls, Waves*, Springer, New York.
[5] Cercignani, C., 2000, *Rarefied Gas Dynamics: From Basic Concepts to Actual Calculations*, Cambridge University Press, New York.
[6] Kärger, J., and Ruthven, D. M., 1992, *Diffusion in Zeolites and Other Microporous Solids*, Wiley, New York.
[7] Cussler, E. L., 1997, *Diffusion: Mass Transfer in Fluid Systems*, 2nd ed., Cambridge University Press, New York.
[8] McCullough, E. A., Kwon, M., and Shim, H., 2003, "A Comparison of Standard Methods for Measuring Water Vapour Permeability of Fabrics," Meas. Sci. Technol., **14**(8), pp. 1402–1408.
[9] Mantle, M. D., Reis, N. C., Griffiths, R. F., and Gladden, L. F., 2003, "MRI Studies of the Evaporation of a Single Liquid Droplet From Porous Surfaces," Magn. Reson. Imaging, **21**(3–4), pp. 293–297.
[10] Manz, B., Chow, P. S., and Gladden, L. F., 1999, "Echo-Planar Imaging of Porous Media With Spatial Resolution Below 100 $\mu$m," J. Magn. Reson., **136**(2), pp. 226–230.
[11] Findley, M. E., Tanna, V. V., Rao, Y. B., and Yeh, C. L., 1969, "Mass and Heat Transfer Relations in Evaporation through Porous Membranes," AIChE J., **15**(4), pp. 483–489.
[12] Pietrass, T., 2006, "Carbon-Based Membranes," MRS Bull., **31**(10), pp. 765–769.
[13] Sholl, D. S., and Ma, Y. H., 2006, "Dense Metal Membranes for the Production of High-Purity Hydrogen," MRS Bull., **31**(10), pp. 770–773.
[14] Perry, J. D., Nagai, K., and Koros, W. J., 2006, "Polymer Membranes for Hydrogen Separations," MRS Bull., **31**(10), pp. 745–749.
[15] Ghali, K., Ghaddar, N., and Jones, B., 2002, "Empirical Evaluation of Convective Heat and Moisture Transport Coefficients in Porous Cotton Medium," ASME Trans. J. Heat Transfer, **124**(3), pp. 530–537.
[16] Johnson, D. W., Yavuzturk, C., and Pruis, J., 2003, "Analysis of Heat and Mass Transfer Phenomena in Hollow Fiber Membranes Used for Evaporative Cooling," J. Membr. Sci., **227**(1–2), pp. 159–171.
[17] Gibson, P., Schreuder-Gibson, H., and Rivin, D., 2001, "Transport Properties of Porous Membranes Based on Electrospun Nanofibers," Colloids Surf., A, **187**, pp. 469–481.
[18] Chen, G., 2005, *Nanoscale Energy Transport and Conversion: A Parallel Treatment of Electrons, Molecules, Phonons, and Photons*, Oxford University Press, New York.
[19] Pollard, W. G., and Present, R. D., 1948, "On Gaseous Self-Diffusion in Long Capillary Tubes," Phys. Rev., **73**(7), pp. 762–774.
[20] Present, R. D., 1958, *Kinetic Theory of Gases*, McGraw-Hill, New York.
[21] Churaev, N. V., and Galwey, A. K., 2000, *Liquid and Vapor Flows in Porous Bodies: Surface Phenomena*, Gordon and Breach, Amsterdam.
[22] Luo, G., Malkova, S., Yoon, J., Schultz, D. G., Lin, B., Meron, M., Benjamin, I., Vanysek, P., and Schlossman, M. L., 2006, "Ion Distributions Near a Liquid-Liquid Interface," Science, **311**(5758), pp. 216–218.
[23] Collier, J. G., and Thome, J. R., 1994, *Convective Boiling and Condensation*, 3rd ed., Oxford University Press, New York.
[24] Lock, G. S. H., 1994, *Latent Heat Transfer: An Introduction to Fundamentals*, Oxford University Press, New York.
[25] Sholl, D. S., 2006, "Understanding Macroscopic Diffusion of Adsorbed Molecules in Crystalline Nanoporous Materials Via Atomistic Simulations," Acc. Chem. Res., **39**(6), pp. 403–411.
[26] Holt, J. K., Park, H. G., Wang, Y., Stadermann, M., Artyukhin, A. B., Grigoropoulos, C. P., Noy, A., and Bakajin, O., 2006, "Fast Mass Transport Through Sub-2-Nanometer Carbon Nanotubes," Science, **312**(5776), pp. 1034–1037.
[27] Eijkel, J. C. T., Dan, B., Reemeijer, H. W., Hermes, D. C., Bomer, J. G., and van den Berg, A., 2005, "Strongly Accelerated and Humidity-Independent Drying of Nanochannels Induced by Sharp Corners," Phys. Rev. Lett., **95**(25), p. 256107.

[28] Heitjans, P., and Kärger, J., 2005, *Diffusion in Condensed Matter: Methods, Materials, Models*, Springer, New York.
[29] Ullal, C. K., Maldovan, M., Thomas, E. L., Chen, G., Han, Y. J., and Yang, S., 2004, "Photonic Crystals Through Holographic Lithography: Simple Cubic, Diamond-Like, and Gyroid-Like Structures," Appl. Phys. Lett., **84**(26), pp. 5434–5436.
[30] ASTM, 1999, "Standard Test Methods for Water Vapor Transmission of Materials: Upright Cup Method," American Society for Testing and Materials Annual Book of ASTM Standards, Part 3.01, ASTM E, 96, Procedure B, Conshohocken, PA.
[31] Traum, M. J., 2007, "Latent Heat Fluxes Through Nano-Engineered Porous Materials," Ph.D. thesis, Massachusetts Institute of Technology, Cambridge, MA.
[32] Cravalho, E. G., and Smith, J. L., 1981, *Engineering Thermodynamics*, Pitman, Boston, pp. 522.
[33] Whitaker, S., 1977, *Fundamental Principles of Heat Transfer*, Pergamon, New York.
[34] Mills, A. F., 1999, *Basic Heat and Mass Transfer*, 2nd ed., Prentice-Hall, Englewood Cliffs, NJ.
[35] Satterfield, C. N., 1991, *Heterogeneous Catalysis in Industrial Practice*, 2nd ed., McGraw-Hill, New York.
[36] Deen, W. M., 1998, *Analysis of Transport Phenomena*, Oxford University Press, New York.
[37] Mills, A. F., 1999, *Basic Heat Transfer*, 2nd ed., Prentice-Hall, Englewood Cliffs, NJ.
[38] Tritton, D. J., 1977, *Physical Fluid Dynamics*, Van Nostrand Reinhold, New York.